Periodic dynamics, localization metastability, and elastic interaction of colloidal particles with confining surfaces and helicoidal structure of cholesteric liquid crystals

Michael C. M. Varney,[1] Qiaoxuan Zhang,[1,2] Mykola Tasinkevych,[3,4] Nuno M. Silvestre,[5] Kris A. Bertness,[6] and Ivan I. Smalyukh[1,2,7,8,*]

[1]*Department of Physics, University of Colorado at Boulder, Boulder, Colorado 80309, USA*
[2]*Materials Science and Engineering Program, University of Colorado at Boulder, Boulder, Colorado 80309, USA*
[3]*Max-Planck-Institut für Intelligente Systeme, D-70569 Stuttgart, Germany*
[4]*Institut für Theoretische Physik IV, Universität Stuttgart, D-70569 Stuttgart, Germany*
[5]*Centro de Física Teórica e Computacional and Faculdade de Ciências da Universidade de Lisboa, Av. Prof. Gama Pinto 2, 1649-003 Lisboa, Portugal*
[6]*National Institute of Standards and Technology, Boulder, Colorado 80305, USA*
[7]*Department of Electrical, Computer, and Energy Engineering and Liquid Crystals Materials Research Center, University of Colorado at Boulder, Boulder, Colorado 80309, USA*
[8]*Renewable and Sustainable Energy Institute, National Renewable Energy Laboratory and University of Colorado at Boulder, Boulder, Colorado 80309, USA*

(Received 20 August 2014; published 4 December 2014)

Nematic and cholesteric liquid crystals are three-dimensional fluids that possess long-range orientational ordering and can support both topological defects and chiral superstructures. Implications of this ordering remain unexplored even for simple dynamic processes such as the ones found in so-called "fall experiments," or motion of a spherical inclusion under the effects of gravity. Here we show that elastic and surface anchoring interactions prompt periodic dynamics of colloidal microparticles in confined cholesterics when gravity acts along the helical axis. We explore elastic interactions between colloidal microparticles and confining surfaces as well as with an aligned ground-state helical structure of cholesterics for different sizes of spheres relative to the cholesteric pitch, demonstrating unexpected departures from Stokes-like behavior at very low Reynolds numbers. We characterize metastable localization of microspheres under the effects of elastic and surface anchoring periodic potential landscapes seen by moving spheres, demonstrating the important roles played by anchoring memory, confinement, and topological defect transformation. These experimental findings are consistent with the results of numerical modeling performed through minimizing the total free energy due to colloidal inclusions at different locations along the helical axis and with respect to the confining substrates. A potential application emerging from this work is colloidal sorting based on particle shapes and sizes.

DOI: 10.1103/PhysRevE.90.062502 PACS number(s): 61.30.Jf, 82.70.Dd, 61.30.Mp

I. INTRODUCTION

Fall experiments, in which a body is allowed to fall under the effect of gravity, have a long and illustrious history, including early experiments from the sixth century on dropping balls of different masses [1], which were refined in the 16th and 17th centuries by Steven and Galileo, respectively [2,3]. Fall experiments do not strictly require an unconstrained falling mass and examples include the famous perturbed or deformed Eötvös experiments [4,5] as well as the present-day tests of equivalency, "big G" measurements, and tests of the gravitational inverse square law [6–9]. Different versions of fall experiments have also been applied to many other physical systems, ranging from characterization of colloids [10] to elementary particle charge and mass measurements [11]. In the field of soft condensed matter physics, such experiments include the studies of rheological properties of nematic and cholesteric liquid crystals (LCs) [12–14].

Fall experiments are relatively simple to perform in LC hosts provided that the colloidal particle is located in the bulk of the LC, far away from topological defects or confining surfaces. Usual experimental procedure is to allow a colloid to settle to a location within the sample volume, then subsequently invert the sample cell and allow the colloid to fall under the influence of gravity. Optical manipulations, via optical tweezers, allow one to move a colloid to positions of interest within the cell [15,16]. However, optical manipulation has many drawbacks, such as being limited to optically transparent systems, and to systems where the elastic forces in regions of interest are less than 10–100 pN, the range of forces typically generated by optical tweezers [15,16]. Furthermore, optical manipulation can often affect local director structure through the realignment of LC molecules and can modify the very structures one wishes to explore. Recent progress in noncontact manipulation, such as magneto-optical holonomic control of colloids [15], allows for robust manipulation of magnetic and optical colloidal handles (MOCH) used to directly probe topological defects and LC structure near confining surfaces.

In this work, we use a magneto-optical manipulation system to perform fall experiments with MOCHs in a cholesteric liquid crystal (CLC), manipulating these particles close to confining surfaces and within the bulk of the CLC in the Stokes flow regime. We find that, contrary to an expected linear fall motion of a colloidal particle balanced by viscous forces at low Reynolds numbers, particles with tangential surface anchoring exhibit periodic dynamics and metastable states in the CLC. This behavior is enhanced by the so-called

*ivan.smalyukh@colorado.edu

"anchoring memory effect" [17–21] of orientational director pinning at the colloidal surfaces as well as by energetic barriers associated with topological defect transformation. We also study elastic interactions of colloidal particles with the confining surfaces of CLC cells, demonstrating elastic levitation of the particles at a well-defined "levitation" level above the bottom cell substrate.

II. MATERIALS, METHODS, AND TECHNIQUES

A. Holonomic optical and magnetic manipulation

Our work uses an integrated magnetic and holographic optical manipulation system [15], which allows us to manipulate MOCH in a fully holonomic manner, i.e., in all three Cartesian degrees of freedom via holographic optical tweezers (HOT), and in all three rotational degrees of freedom via magnetic control. Holographic optical tweezers allow us to exert well-controlled forces (commonly within the range of 0.1–100 pN) and to reliably position and spatially translate individual particles or their arrays in three dimensions. Magnetic fields can exert strong torques on ferromagnetic or superparamagnetic colloids [15,22–24] in a highly controllable manner. This allows us to explore the structural landscape within a cholesteric sample volume, including near to and within topological defects, and near confining surfaces, such as glass cell walls [15].

Our integrated holonomic magnetic and holographic optical manipulation system is shown in Fig. 1(a). Magnetic manipulation is achieved using three electromagnets (Fisher Scientific Company model S52051 [25]) composed of solenoids in which custom machined cast iron cores have been inserted. These magnets are arranged on an orthogonal x-y-z Cartesian coordinate system and mounted to a frame machined from aluminum and then positioned on an inverted Olympus microscope [15]. A microscope slide holder machined from aluminum is positioned in the x-y plane using precision translation stages. Each electromagnet is independently driven via an amplified power supply (APS) (Kepco model BOP20-5M [25]) and is voltage controlled using a computer-controlled device acquisition card (National Instruments USB-6259 BNC) and in-house LABVIEW-based software (LABVIEW was purchased from National Instruments [25]). Each electromagnet can produce ac (up to 8 Hz) and/or dc magnetic fields up to about 40 G. The influence of up to 110 G magnetic fields (used in all magnetic manipulations presented herein) on the LC director $\mathbf{n}(\mathbf{r})$ may be neglected because director realignment is typically a thresholdlike effect and requires fields $\sim$1000 G at our studied cell thickness values, in agreement with our experimental observations.

The magnetic colloids in our work are superparamagnetic beads (SPMBs) (Dynabead M450, obtained from Invitrogen [25]) with a nominal diameter of 4.5 μm $\pm$ 0.1 μm and a density of $\sim$1.9 g/cm^3 [15]. These beads are fabricated using ferromagnetic nanoparticles (γ Fe_2O_3 and Fe_3O_4) approximately 8 nm in diameter that are embedded into a highly cross-linked epoxy with a density of $\sim 10^5$ nanoparticles per bead. Random orientation of individual ferrite nanoparticles, coupled with thermal moment flipping, creates a zero net magnetic moment in the SPMB. When an external magnetic field $\mathbf{H}$ is applied, a net magnetic moment $\mathbf{m}$ is induced in the SPMB [26]:

$$\mathbf{m} = V_p \chi_p \mathbf{H}, \tag{1}$$

where V_p is the SPMB volume and χ_p is its effective magnetic susceptibility. Subsequent rotation of the external magnetic field $\mathbf{H}$ generates a torque on the SPMB given by [23]

$$\boldsymbol{\tau} = \mu \mathbf{m} \times \mathbf{H}, \tag{2}$$

where μ is the colloid's magnetic permeability. Superposition of magnetic fields from each solenoid allows us to set $\mathbf{H}$ in any direction and also to rotate this field at a given frequency, allowing us to achieve desired angular rotation of MOCHs. Since our experiment deals with low Reynolds number flow, on the order of Re $\sim 10^{-7}$, we neglect inertial effects and quantify the magnitude of the torque $\tau \equiv |\boldsymbol{\tau}|$ acting on the SPMB by balancing it with the viscous torque in the LC host [27–29] opposing this rotational motion,

$$\tau = \left(\frac{4\pi}{3}\right) \alpha R^3 \eta \Omega_c, \tag{3}$$

where R is the SPMB radius, η is the effective viscosity coefficient of the LC host, Ω_c is the critical decoupling frequency of the sphere rotation with respect to the external

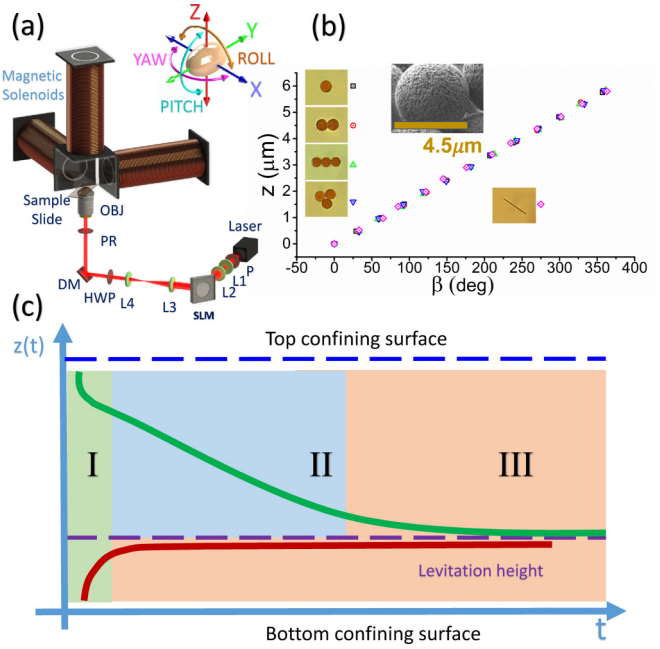

FIG. 1. (Color online) (a) Solenoids arranged in a Cartesian aluminum frame mounted on an inverted microscope (not shown) coupled to an optical imaging system capable of both POM and 3PEF-PM imaging. (b) Colloid center-of-mass position along the cholesteric helical axis $\boldsymbol{\chi}$ (which is aligned along the z axis) vs relative rotation angle β for multiple colloid species (SPMB and GaN nanowire) in various configurations. The inset is a SEM image of a SPMB showing surface roughness. (c) Predicted dynamics of SPMB in a CLC cell when only gravitational and elastic particle-substrate interactions are present. Region I denotes a so-called "wind-up and lift-off," Region II denotes a "fall" region, and Region III is the "levitation" regime.

magnetic field rotational frequency, and α is a numerical factor on the order of unity. Using this approach, we measured a magnetic torque magnitude of $\tau \sim 5 \times 10^{-18}$ N m exerted on the SPMB at ~100 G fields in various LCs [15]. When operated in the x-y plane configuration, the finite radius of the solenoid cores results in a residual in-plane field gradient that yields residual forces of up to 0.07 pN at 100 G, which is comparable to the gravitational force acting on these particles while dispersed in the CLC.

Full holonomic control of a colloidal particle is achieved by combining mostly rotational magnetic manipulation with translational manipulation by HOT using a single integrated setup shown in Fig. 1(a). The HOT is built using a fiber laser operating at 1064 nm with output powers of up to 10 W. The trapping beam passes through a polarizer (P) and two lenses (L1, L2) that form a telescope that is used to resize the beam diameter to slightly overfill the active area of a computer-controlled, dynamically addressable, LC-based spatial light modulator (SLM). After modulation by the SLM, the trapping beam is linearly polarized in a desired orientation using a half-wave retardation plate and a polarizer and subsequently directed via a second telescope (L3, L4) and reflection from a dichroic mirror to the back aperture of a 100× oil immersion objective with a numerical aperture NA = 1.42. Imaging is done through a combination of polarizing optical microscopy (POM) and three-photon epifluorescence polarizing microscopy (3PEF-PM) that are capable of operating in both epidetection and forward-detection (transmission) modes, with the epidetection mode being the primary configuration when implementing full three-axis holonomic manipulation.

B. Sample preparation

We create a CLC from a commercial single-compound nematic LC pentylcyanobiphenyl (5CB, obtained from Frinton Labs) doped with a small volume fraction of chiral agent cholesteryl pelargonate (purchased from Aldrich Chemistry [25]) to obtain cholesteric pitch in the range of 2.5–10 μm. In addition to the SPMBs discussed previously, we also use GaN nanowires of two species, one coated with aluminum and the other uncoated (NIST lots C004 and C144, respectively). Such nanowires were described in detail in previous work [30]. All colloidal particles are dispersed in a CLC host via either solvent exchange or sedimentation mixing [15], with both methods yielding comparable dispersion efficiencies for SPMBs, and the solvent exchange approach being our method for dispersion of GaN nanowires. Cells are constructed from clean glass slide substrates coated with polyimide to set planar anchoring boundary conditions for $\mathbf{n}(\mathbf{r})$. Cell thickness varies from 30 to 60 μm, depending on the system under study. Our CLC host is infused into these cells via capillary forces and subsequently sealed with fast-setting epoxy.

POM shows that the particles induce tangential (planar) nondegenerate surface anchoring for $\mathbf{n}(\mathbf{r})$ of the LC [15], where the director tends to pin to colloid surfaces by a phenomenon often referred to as "anchoring memory effect." This behavior is consistent with scanning electron microscope (SEM) images [inset of Fig. 1(b)] revealing nonuniform, nanoscale surface morphology that naturally allows for strong coupling between the superparamagnetic beads and the CLC director [17–21]. Such coupling is important in locking the rotation of a colloid to its translation along the CLC helical axis. We find that rotating a colloidal particle by 2π rad around its axis (and the CLC helical axis) induces a translation of one cholesteric pitch along this axis [Fig. 1(b)], a relation that holds for a wide range of colloid species of different size, composition, and configurations, including SPMB monomers and chains and GaN nanowires. This lock between rotation and translation is very strong, allowing us to manipulate SPMBs into contact with confining surfaces despite strong elastic repulsion between the colloidal particle and the surface. Surface anchoring memory effects [17–21] are also key in understanding the origin of the so-called "metastable states" observed in our work, as we will discuss below.

III. RESULTS

A. Regimes of dynamics of colloidal particles

Our previous studies noted a strong coupling [similar to that shown in Fig. 1(b)] between the translation of a colloidal particle along the cholesteric helical axis, and its rotation about this axis [14]. Fall experiments with such particles can be performed by waiting for a colloidal dispersion in a CLC to "settle" under gravitational forces to a so-called "levitation layer" where particle-substrate elastic repulsive and buoyant forces balance with gravitational forces. This allows for characterization of the motion of these colloidal particles along the helical axis, but the motion range is limited due to elastic repulsive forces near the cell surfaces, as it is impossible to gravitationally manipulate colloids below this levitation layer. Furthermore, fall times could be on the order of days, thus limiting the ability to do repeated experiments on a single colloid. HOT manipulation allows one to reposition a given colloid within the cell volume, but (at relatively large laser powers) this could affect the LC structure or the colloid surface properties due to optical realignment of the local director, or thermal heating of the colloid surface [14]. Likewise, there are issues in optically manipulating colloidal particles close to a cell surface, such as thermally induced heating and adhesion of the particle to a glass plate. Magnetic manipulation allows us to position a SPMB anywhere along the helical axis in a CLC, including below levitation layers and even into contact with glass substrate walls without affecting the LC structure or a particle's surface anchoring properties. Additionally we can rapidly move the particle and repeatedly position it at a desired location to study its dynamics [15].

Particle motion within the CLC cell is enriched by elastic forces, which appear in addition to buoyant, viscous drag and gravity forces that are also common for isotropic fluid hosts. These interactions are highly complex, especially elastic interactions between the CLC, the particle, and the confining cell surfaces. An approximation of the particle-substrate elastic force in very-large-pitch CLCs, where pitch is much larger than the colloidal particle's diameter, and approaching the limit of a nematic LC, may be found by an "image charge" approach, similar to what was previously done for nematics [31]. However, as the cholesteric pitch approaches that of the diameter of the particle, elastic interactions with confining surfaces become complex [32,33] and are best

modeled through a combination of experiment and numerical simulations [32–34].

Viscous drag force on a SPMB in the Stokes flow regime is given by [35,36]

$$F_{\text{viscous}} = 6\pi\eta R v_{\text{cm}}, \tag{4}$$

where v_{cm} is the center-of-mass speed of the bead. Finally, the combination of gravity and buoyant force is given by

$$F_{\text{gravity\_reduced}} = \tfrac{4}{3}\pi R^3 g(\rho_{\text{lc}} - \rho_{\text{spmb}}) \tag{5}$$

where g is Earth's gravitational acceleration and ρ_{lc} and ρ_{spmb} are the LC and SPMB densities (1.38 g/cm^3, 1.9 g/cm^3, respectively.) Balancing the above forces and numerically simulating the elastic forces can fully characterize the motion of a bead. However, it is instructive to first consider the equation of motion within motion regimes described below that neglect the complexity of the bead's interaction with the cholesteric structure.

We can roughly define three regions where one expects different dynamics in the fall experiment [Fig. 1(c)]: Region I we name the "wind-up and lift-off" regime, Region II the "fall" regime, and Region III the "levitation" regime. In Region I, a wind-up consists of magnetically rotating a SPMB, thus translating it along the vertical helical axis until it barely comes into physical contact with either the top or bottom cell substrate. A lift-off occurs when the magnetic field is shut off and the SPMB is repelled from the substrate due to the elastic force of interaction between the SPMB and the substrate. In Region II, since the Reynolds number is small, when disregarding elastic interactions, the SPMB would naïvely be expected to move as dictated by balancing the viscous drag [Eq. (4)] and buoyant/gravitational forces [Eq. (5)]:

$$v_{\text{cm}} = dz/dt = 2R^2 g(\rho_{\text{lc}} - \rho_{\text{spmb}})/(9\eta). \tag{6}$$

This equation has the expected linear solution characteristic of fall experiments in isotropic fluids in the Stokes flow regime. We note, however, that very thick cells would be required for elastic forces of repulsion from confining substrates to be smaller or negligible as compared to gravity forces, and even then Region II dynamics can be realized only within the central part of the LC cell's vertical cross section. As the SPMB continued its fall, it would transition to Region III while repelling elastically from the bottom cell wall. Although the actual observed motion of particles in confined CLCs is much more complicated, below we will distinguish three analogous regimes I–III that describe different types of more complex particle dynamics.

B. Metastable states in CLCs

To quantify the dynamics of colloidal particles in CLCs, we introduce SPMBs into a 5CB-based cholesteric with a pitch of 5 μm (as verified via 3PEF-PM imaging). This CLC colloidal dispersion is infused into a planar rubbed cell of thickness $h \approx 30\,\mu$m. We let the cell relax for several hours to days, depending on cell thickness, so as to minimize the number of topological defects present in the sample, which can interact with and trap SPMBs within their defect cores, as well as distort the local helical axis. For our experiments, we selected SPMB spheres with visible surface features, such as a small protrusion, in order to enhance video image tracking and analysis. Using our magnetic manipulation system alone, we rotated the SPMB at 0.25 Hz and 100 G in a clockwise direction as seen in the inverted microscope visual field, which translated the colloidal particle along the CLC helical axis towards the top confining surface (exploiting the left-handed structural organization of the CLC). We continued this rotation until the SPMB made physical contact with the cell surface, at which point we switched off the magnetic field and observed the motion of the SPMB through the entire cross section of the cell.

The most striking finding is the periodic dynamics and metastable states present in Region II (Fig. 2). In contrast to a linear Stokes flow motion that could be expected in this regime, assuming no elastic interactions present, we noted periodic dynamics where the SPMB would rapidly rotate, then slow its rotation for a certain period of time before returning to its former, higher rotation rate. This behavior repeats, each instance with a spatial period of one cholesteric pitch and a somewhat constant temporal period of approximately 1000 s. The SPMB subsequently settles at its levitation height of approximately 26 μm from the top substrate.

The origin of these metastable states lies in the tangential surface anchoring of molecules on the SPMB surface and is enhanced by the anchoring memory effect [19] wherein particles induce strong tangential (planar) nondegenerate surface boundary conditions for $\mathbf{n}(\mathbf{r})$, causing local director pinning to particle surfaces. As the SPMB particle falls under gravity, this strong pinning hinders rotation of the bead, storing energy in the surrounding CLC elastic field and in deviations of the director at the particle's surface from the easy axis, as well as dilating or compressing the cholesteric pitch around the SPMB. When the free-energy density increase becomes large enough, the pinned director "slips" along the colloid surface, partially relieving the distortion of the director field and allowing the SPMB to rapidly relax to a new, lower energy position within the cell. This process is further enhanced by distortions of cholesteric layered structure around the sphere and repeats until elastic repulsion from the bottom cell wall balances all other forces, and the SPMB ceases its rotation in the sedimentation layer.

C. Particle-wall elastic interactions

Analysis of Region I dynamics due to interaction of the SPMB with the cell substrates (Fig. 3) shows the center-of-mass motion due to a combination of the dominant elastic repulsion near the top and bottom confining surfaces and the much weaker gravitational and buoyant forces. For the top confining surface [Fig. 3(a)], an exponential fit of the angular rotation vs time yields a time constant of ≈21.3 s (fitting is good, with a coefficient of determination of 0.98). The inset plot is the time derivative of this exponential fit and indicates that the initial particle speed is 0.18 μm/s, after which the speed exponentially decays.

Colloidal particle motion near the bottom substrate surface is shown in Fig. 3(b), along with an exponential fit of experimental data yielding a time constant ≈11.9 s, with the inset again showing an initial lift-off speed of ∼0.18 μm/s, but undergoing a slightly faster exponential decay. The apparent asymmetry in dynamics and the difference in time constants

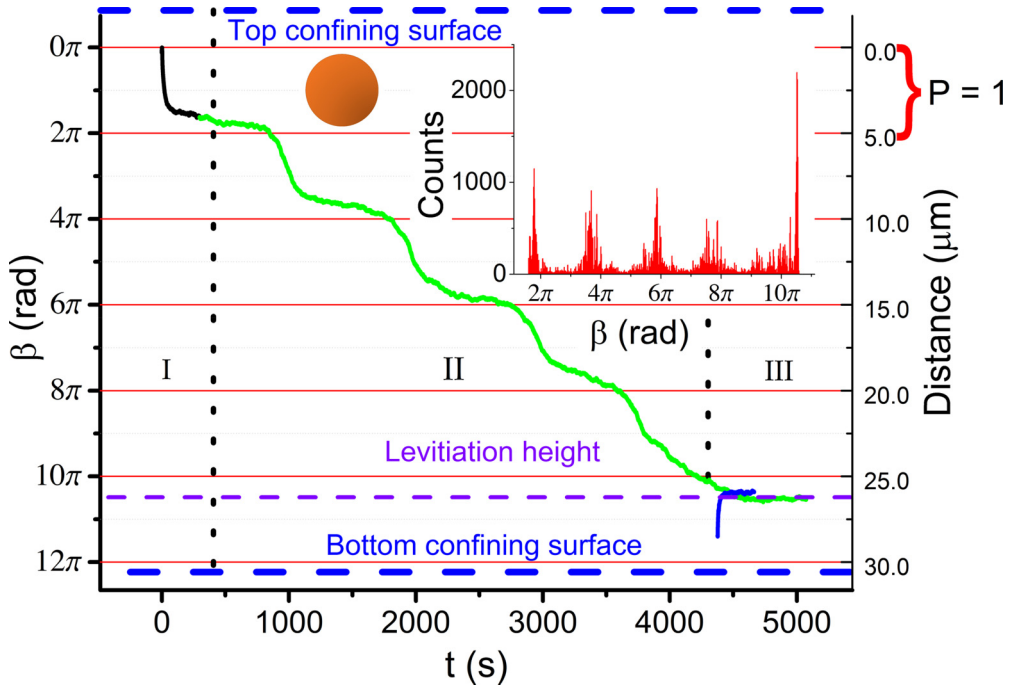

FIG. 2. (Color online) Metastable states evident in a $P = 5\,\mu$m CLC infused in a $h \approx 30\,\mu$m planar aligned cell. (Region I) A SPMB is wound up to the top cell surface using magnetic manipulation and then released. The inset plot shows a histogram of the number of counts per 3° bin over the range of Region II metastable states. The blue and black solid curves (Regions I and III respectively) shows the repulsive motion of the center of mass of the colloidal particle away from the bottom and top confining surfaces, respectively. Note that the colloidal particle shown is scaled to the cholesteric pitch corresponding to 2π rotation. The right vertical axis represents the distance traveled by the colloidal particle's center of mass from its original position at the top cell wall.

describing the behavior at the top and bottom confining surfaces can be explained by gravity acting on the colloidal particle. If there were no gravitational forces at work, and assuming the elastic repulsion of a particle from the top and bottom confining surfaces were equal, we would expect the time constants for the top and bottom surfaces to be equal as well, with the colloid eventually coming to rest in an overdamped manner at the cell midplane. Elastic interactions with the bottom confining surface are balanced by the buoyant and gravitational forces acting on the SPMB, leading to levitation above the bottom confining surface. However, near the top confining surface the directionality of the gravitational and dominant elastic forces acting on the microsphere coincide, and thus, the particle fall from the top surface is free to transition continuously from Region I to Region II, in contrast to repulsion from the bottom substrate.

D. Effects of particle size relative to the cholesteric pitch

We further explored metastable states and periodic dynamics in cells composed of SPMB dispersed into a 5CB-based CLC with a pitch of 2.5 μm (verified via a direct 3PEF-PM imaging) infused into a planar cell of thickness $h \approx 60\,\mu$m. We again obtained metastable states (Fig. 4). Interestingly, a larger number of metastable states were observed (which is due to the higher cell thickness to pitch ratio), and the well-pronounced elastic repulsion from a cell wall was observed over many more CLC layers as compared to that in a cell with $P = 5\,\mu$m. Additionally, in contrast to the behavior seen in Fig. 2, metastable states were apparent even in Region I, as seen in Fig. 4. To emphasize this behavior, the inset in Fig. 4 was obtained by noting the points with the same phase of the SPMB rotational motion shown in Fig. 4. The angular rotations corresponding to these points vs time are plotted in the inset of Fig. 4 and can be characterized by an exponential fit of time constant of about 2390 s over the first six to eight pitches. A linear fit of the remaining prelevitation data points indicated that at times ~5000 s and beyond elastic interactions with the surfaces were no longer dominant, giving an average fall speed of approximately 0.002 μm/s. We note that elastic interaction with the bottom confining surface was likewise enhanced, leading to a levitation region approximately 38 μm from the top confining surface of the $h \approx 60\,\mu$m cell. This indicates a strong pitch dependence of the particle-wall repulsive elastic force.

We finally explored formation of metastable states and periodic dynamics in large-pitch cholesterics by use of SPMB dispersed into a 5CB-based CLC with $P = 10\,\mu$m infused into a planar rubbed cell with thickness $h \approx 60\,\mu$m. Figure 5 shows that metastable states are present, and exhibit a linear periodicity in both time and pitch. The levitation is observed at a distance $\approx 44\,\mu$m from the particle's initial location at the top surface of the $h \approx 60\,\mu$m cell (Fig. 5). These results indicate that metastable states exist in CLCs with a wide range of pitch and cell thickness values. We note, finally, that direct comparisons of levitation height and CLC pitch are possible only for the $P = 2.5\,\mu$m and $P = 10\,\mu$m CLCs as they are in cells of the same thickness, $h \approx 60\,\mu$m (the $P = 5\,\mu$m CLC is in a cell of $h \approx 30\,\mu$m, which also alters the nature of elastic interactions with confining surfaces).

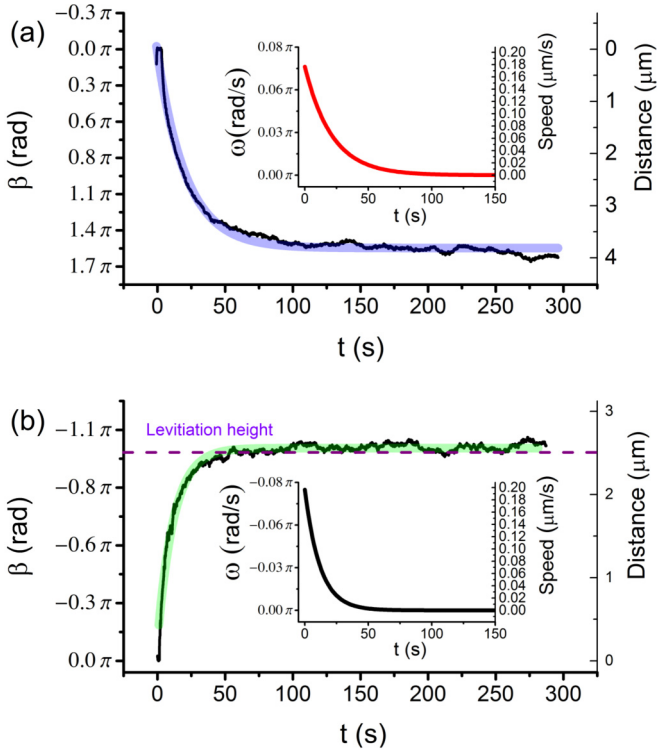

FIG. 3. (Color online) Elastic repulsion of a SPMB from cell surfaces in a $P = 5\,\mu$m CLC infused into a $h \approx 30\,\mu$m planar aligned cell. (a) Analysis of the Region I top cell wall lift-off from Fig. 2. An exponential fit yields a time constant of ≈21.3 s. The inset is the time derivative of this fit. (b) Analysis of the Region I bottom cell wall lift-off from Fig. 2. An exponential fit yields a time constant of ≈11.9 s. The inset is the time derivative of this fitting curve. The dashed line indicates the "levitation height" where the elastic repulsion between the SPMB and the cell wall balance the buoyant and gravitational forces.

E. Effects of particle shape and topography

The above results suggest that metastable states and periodic particle dynamics in CLCs might be influenced by anchoring memory effects on SPMB surfaces. It is well known [18–21] that the anchoring memory effect is determined by material characteristics along with the surface topography. In order to explore the effect of topography on metastable state formation, we selected SPMBs with obvious differences in surface characteristics, including defects such as spherical extrusions from their surface or those with deliberately laser-induced minor surface damage. Such surface imperfections are expected to effectively increase the coupling of the director structure to the particle surface and effectively reduce the symmetry of the colloid, which, in turn, should enhance formation of metastable states. Figure 6 quantifies a SPMB with a spherical extrusion located in our $P = 2.5\,\mu$m CLC infused into an $h \approx 60\,\mu$m cell. Note the differences between metastable states observed for this colloidal particle and the one shown in Fig. 4 within the same time span. The metastable states are indeed much more apparent and longer lived in the experiment shown in Fig. 6.

The effects of shape and topography of colloidal particles were also studied by performing fall experiments on SPMB

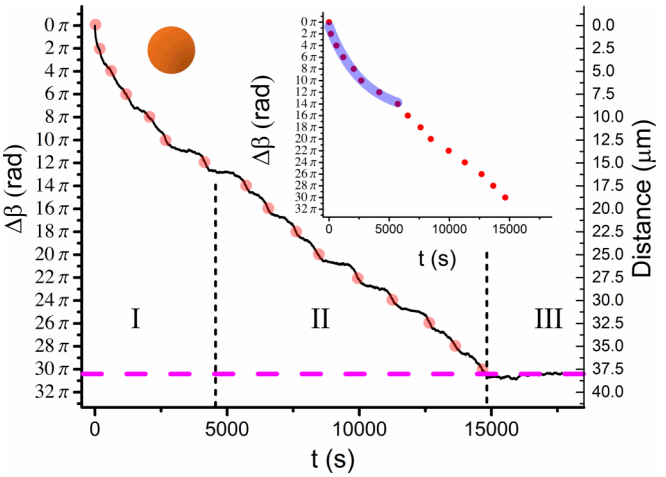

FIG. 4. (Color online) Metastable states evident in a $P = 2.5\,\mu$m CLC infused in a $h \approx 60\,\mu$m planar cell. A SPMB is wound up to the top cell surface using magnetic manipulation and released, subsequently undergoing an elastically mediated lift-off from the cell surface followed by periodic dynamic metastability with an angular periodicity of 2π rad, or one cholesteric pitch. Unlike in the $P = 5\,\mu$m CLC, periodic dynamic metastability is apparent even close to substrates. In the inset, the elastic interaction between the colloid and the top confining surface is highlighted by locating the intercept points at each cholesteric pitch [red (gray) circles] and plotting them with respect to time. Data between $0 < \Delta\beta < 12\pi$ rad (Region I) are fitted with an exponential function of time constant of about 2870 s. A linear fit with a slope of 0.005 rad/s (0.002 μm/s) is used for Region II, or $\Delta\beta \geqslant 10\pi$ rad. Note that the colloidal particle is scaled to cholesteric pitch.

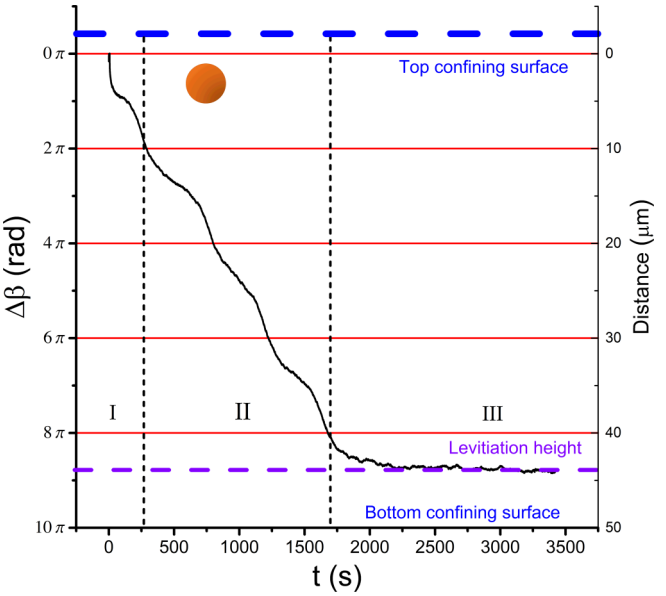

FIG. 5. (Color online) Metastable states evident in a $P = 10\,\mu$m CLC infused in a $h \approx 60\,\mu$m planar aligned cell. A SPMB is wound up to the top cell surface using magnetic manipulation and released, undergoing an elasticity-mediated lift-off from the cell surface followed by "metastable states" with an angular periodicity of 2π rad, or one cholesteric pitch. The strongly pronounced elastic repulsion of the SPMB from the top surface extends within about one cholesteric pitch. Note that the colloidal particle is scaled to cholesteric pitch.

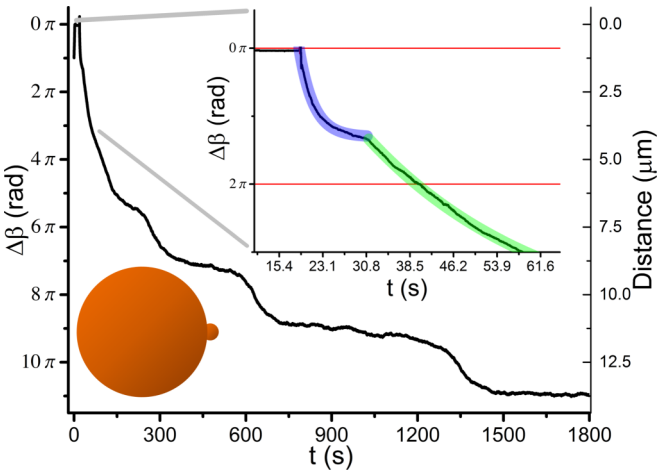

FIG. 6. (Color online) Particle topography enhancement of metastable states in a $P = 2.5\,\mu$m CLC infused in a $h \approx 60\,\mu$m planar aligned cell. A SPMB with a spherical protrusion of diameter $\sim\frac{1}{15}$ of that of the bead enhanced the metastable states. The inset shows the region of elastic repulsion from the cell wall. Note that the colloidal particle in the inset is scaled to pitch.

dimers (an assembly of two SPMBs in contact). Such a dimer located within the CLC sample often has its center-to-center axis tilted with respect to the cholesteric layer (and the plane of the cell) by approximately 10°–15° and can be magnetically manipulated. Upon undergoing a fall, the colloidal dimer exhibited periodic dynamics and metastable states that had a distinct "double bump" signature, as seen in Fig. 7. This behavior can be qualitatively understood as a superposition of the metastable states of two separate spherical colloids shifted with respect to each other along the helical axis and mechanically coupled to each other. Thus, the dynamics of colloids in cholesterics is expected to become even more complex as the topological and topographical complexity of the colloid is increased.

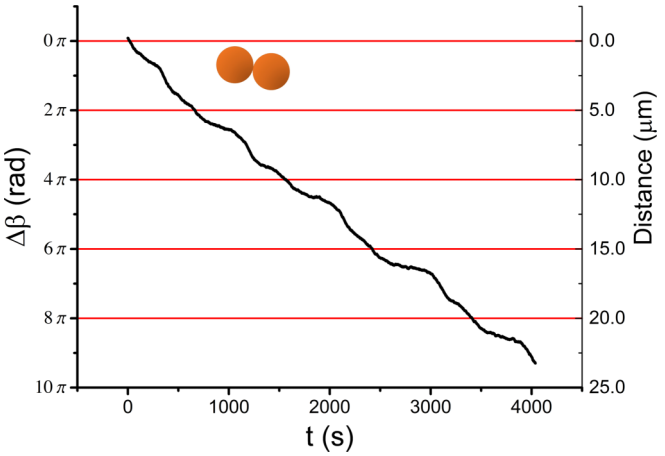

FIG. 7. (Color online) Fall experiments with SPMB dimer. A SPMB dimer in 5-μm-pitch CLC is allowed to fall in Region II in a $h \approx 30\,\mu$m cell. The dimer tends to situate at an angle of 10°–15° with respect to the plane of the CLC lamella. This dependence exhibits a distinct "double period" and the corresponding metastable states.

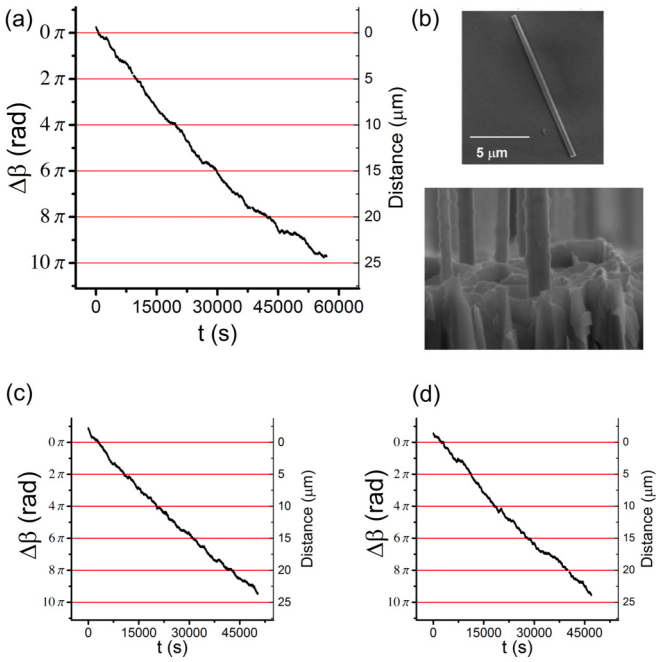

FIG. 8. (Color online) Fall experiments with uncoated and coated GaN nanowires in a $P = 5\,\mu$m CLC infused in a $h \approx 60\,\mu$m cell. (a) Fall data for an uncoated GaN nanowire of nominal length of 10 μm and 350 nm diameter with planar anchoring. (b) SEM images of (top) an uncoated GaN nanowire and (bottom) Al-coated GaN nanowires with nanopyramidlike surface structures. (c) Fall data for an Al-coated GaN nanowire of nominal length of 10 μm and 350 nm diameter show that the metastable states are suppressed. (d) The data for Al-coated GaN nanowire after three weeks exhibit weakly pronounced metastable states.

In order to further quantify topographical shape and/or size effects on the observed periodic dynamics, we performed fall experiments with uncoated and Al-coated GaN nanowires (Fig. 8). An uncoated GaN nanowire [shown in the top part of Fig. 8(b)] imposes planar anchoring with the easy axis along the long axis of the wire [14]. Since our GaN wires are not magnetically responsive, we are unable to use magnetic manipulation and thus are unable to explore the colloidal particle behavior very near confining surfaces. However, by judicious use of HOT to position a nanowire far from topological defects, and after allowing the GaN nanowires to sediment towards one surface, we inverted the cell and observed the nanowire falling under gravity over a period of 12 h. Weakly pronounced metastable states can be seen in Fig. 8(a) for the uncoated GaN wire depicted in the top part of Fig. 8(b).

An Al-coated GaN nanowire [depicted in the bottom of Fig. 8(b)] is observed to initially have poorly defined anchoring when first infused into our CLC host. A suppression of metastable states is observed in LC samples "freshly infused" with such Al-coated nanowires [Fig. 8(c)]. This may be due to Al nanopyramids with a nominal base dimension of 100 nm and a height of ∼100 nm that form at random locations on the facets of the GaN nanowire during coating, having a tendency to further randomize the local anchoring and, thus, suppress the metastable states. However, this behavior is transient. After

several weeks, the nanopyramid-induced distortions relax so that the nanowires align along the far-field director of a nematic host and the weak periodic dynamics in the fall experiment in CLCs reappears [Fig. 8(d)].

F. Numerical modeling of SPMBs in a cholesteric liquid crystal

To explore the energetics and symmetry breaking effects that result in the periodic particle dynamics and metastable states in CLCs, we numerically minimize the total free energy due to the incorporation of a spherical colloidal particle in the CLC bulk far away and close to a confining surface. The Landau–de Gennes phenomenological description is based on a traceless, symmetric rank-3 tensorial order parameter $Q_{ij}(i,j=1,\ldots,3)$, which has five independent components. In the one elastic constant approximation, the Landau–de Gennes free energy of a representative chiral nematic may be written as [35,36]

$$F_{\mathrm{LdG}} = \int_V \left[a Q_{ij}^2 - b Q_{ij} Q_{jk} Q_{ki} + c\left(Q_{ij}^2\right)^2 + \frac{L}{2} \partial_k Q_{ij} \partial_k Q_{ij} + \frac{4\pi L}{P} \epsilon_{ijk} Q_{il} \partial_j Q_{kl} \right], \quad (7)$$

where a, b, c, are phenomenological material constants, L is a phenomenological parameter related to the Frank elastic constant K, and P is the cholesteric pitch. ϵ_{ijk} is the Levi-Civita symbol, and the Einstein convention for summation over repeated indexes is implied. The constant a (unlike the constants b and c) is assumed to depend linearly on temperature T, and is usually written $a(T) = a_0(T - T^*)$, where a_0 is another material-dependent constant, and T^* is the supercooling temperature of the isotropic phase.

We describe planar degenerate anchoring of the director at colloidal interfaces by the following surface anchoring free energy [37,38]:

$$F_s = W \int_{\partial V} \left[(\tilde{Q}_{ij} - \tilde{Q}_{ij}^{\perp})^2 + \left(\tilde{Q}_{ij}^2 - \frac{3Q_s^2}{2} \right)^2 \right] ds, \quad (8)$$

where $W > 0$ is the anchoring strength favoring both tangential degenerate anchoring of the director, and Q_s is the preferred surface scalar-order parameter; $\tilde{Q}_{ij} = Q_{ij} + Q_s \frac{\delta_{ij}}{2}$, $\tilde{Q}_{ij}^{\perp} = (\delta_{il} - \nu_i \nu_l)\tilde{Q}_{lk}(\delta_{kj} - \nu_k \nu_j)$ with δ_{ij} being the Kronecker delta symbol, and $\boldsymbol{\nu}$ is the unit outward normal vector to the confining surface. The total free energy $F = F_{\mathrm{LdG}} + F_s$ is then minimized numerically by employing the adaptive mesh finite elements method as described in more detail in Ref. [38]. We assume $V = \{0 \leqslant x, y \leqslant L, 0 \leqslant z \leqslant h\}$, and use uniaxial twisted nematic as the initial conditions Q_{ij}^0 for the minimization, i.e., $Q_{ij}^0(z) = \frac{Q^0}{2}(3n_i^0 n_j^0 - \delta_{ij})$ with $(n_x^0, n_y^0, n_z^0) = \{\cos[q_0(h-z)], -\sin[q_0(h-z)], 0\}$, $q_0 \equiv 4\pi/P$. The helical axis is assumed to be in the z direction. At this point we would like to emphasize that in the cholesteric phase the order parameter $\boldsymbol{Q}$ is necessarily biaxial [39]. We always set $h = nP$, where n is an integer, and impose fixed boundary conditions on $\boldsymbol{Q}$ with the values specified by the above expression on Q_{ij}^0 evaluated at the system boundaries ∂V. Following [38,39] we introduce the dimensionless temperature $\tilde{T} \equiv 24a(T)c/b^2$ and the correlation length $\xi = \sqrt{12cL/b^2}$ at the nematic-isotropic ($q_0 = 0$) transition. The cholesteric phase is stable for $\tilde{T} < \tilde{T}_{\mathrm{CI}}$, where the cholesteric-isotropic coexistence temperature is given by [36–38]

$$\tilde{T}_{\mathrm{CI}} = \begin{cases} \frac{1}{2}\{1 + (q_0\xi)^2 + [1 + \frac{1}{3}(q_0\xi)^2]^{\frac{3}{2}}\}, & q_0\xi \leqslant 3 \\ (q_0\xi)^2, & q_0\xi > 3 \end{cases}. \quad (9)$$

We use the following values of the bulk parameters $a_0 = 0.044\,\mathrm{MJ/m^3}$, $b = 0.816\,\mathrm{MJ/m^3}$, and $c = 0.45\,\mathrm{MJ/m^3}$, $L = 6\,\mathrm{pJ/m}$, $T^* = 307\,\mathrm{K}$. The spatial extension of inhomogeneous regions and the cores of topological defects are of the order of the coherence length $\xi \approx 7$ nm. For simplicity we set both Q_s and Q^0 equal to the value of the scalar-order parameter in the bulk nematic phase $Q_N = b(1 + \sqrt{1 - \frac{8\tilde{T}}{9}})/8c$. To mimic the experiments, we use similar ratios between the cholesteric pitch and the particle size while taking smaller effective size and pitch values to reduce the computational time needed for the free-energy minimization, as we describe below.

Figure 9 shows the cholesteric configurations induced by the particles as a function of the pitch relative to the particle size, which is consistent with prior studies of cholesteric director field and layer configurations induced by colloidal inclusions and their assemblies [40–42]. The surface director field features four disclinations of winding number $\frac{1}{2}$, which correspond to two split-core boojums connected by semiloops of two bulk half-integer disclination lines. The length of the disclination line undergoes a rather sharp transition (contrary to previous numerical findings of a smooth variation of the defect length with the pitch [33]) from an extended regime [Fig. 9(a)] for $P \leqslant P^* < 2R$ to a short one for larger values of the pitch [Figs. 9(b)–9(d)]. Very long disclination lines are thermodynamically less stable, and we occasionally observe splitting of such lines via creation of self-compensating $+\frac{1}{2}$ and $-\frac{1}{2}$ pairs of surface disclinations.

Figure 10 summarizes the dependence of the free energy on the distance from the CLC-embedded particle to a confining surface wall. The general feature is an overall repulsion from the wall, with a well-pronounced oscillatory behavior having a period equal to P [see Fig. 10(e)]. The free-energy oscillations are systematic with the amplitude significantly larger than the numerical inaccuracy. This is consistent with our experimental findings of the metastable states and periodic particle dynamics discussed above, which for some R, P, and h parameters were observed even within Region I of particle's repulsion from a confining substrate (Fig. 4). Figures 11 and 12 depict the cholesteric configurations around a colloidal particle as a function of the particle's surface-wall distance d for two values of the cholesteric pitch. It is worth emphasizing that the surface director and the positions of the boojums change and slide around the particle's surface as d changes.

IV. DISCUSSION

One of the classic examples of nontrivial interaction of a cholesteric ground-state structure with surfaces is the so-called "Bouligand arches," a characteristic texture appearing when a flat surface in contact with a cholesteric material is

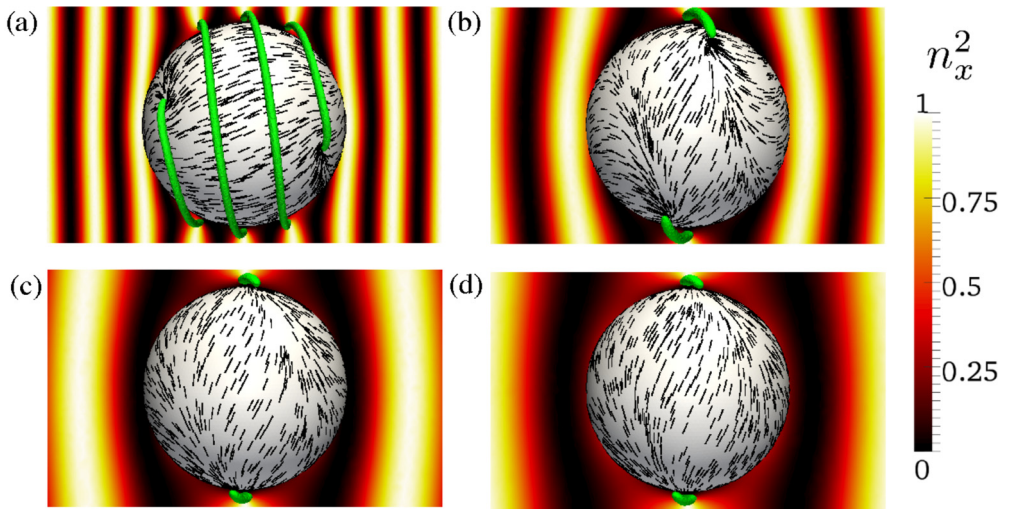

FIG. 9. (Color online) Director configurations at the particle surface and in the bulk around it obtained numerically. Colloidal particle is in the center of the cell and far from confining walls. $L = 2.5P$, $h = 5P$, $R = 0.1\,\mu$m. (a) $P = R$. (b) $P = 2R$. (c) $P = 3R$. (d) $P = 4R$. The color code represents n_x^2, and the isosurfaces of the reduced scalar-order parameter (depicting defects) $Q = 0.25$ are shown using a green color.

at an oblique angle with respect to the helical axis [35,36]. It is not surprising that such Bouligand arches also appear on surfaces of spherical particles in some of the ranges of pitch to particle size ratios [see, for example, Figs. 9(b)–9(d)]. Due to the fact that the closed spherical particle's surface is making continuously varying angles with respect to the helical axis, the pattern of the director on the surface is somewhat more complex, but its origin can be understood in a similar way as that of the Bouligand arches.

Clearly, even when the anchoring on the particle surface is tangentially degenerate, so that only the polar component of the anchoring energy needs to be considered in the interaction of a spherical surface with the helicoidal configuration of the cholesteric host, this interaction is still highly dependent on the particle's center-of-mass position along the helical axis. Bulk elastic distortions of the uniform helicoidal structure are induced and the director at a spherical particle's surface deviates from the easy plane in polar directions, resulting in both surface anchoring and bulk elastic free-energy costs in a particle-medium interaction. Furthermore, the structure of topological defects (boojums and surface disclinations) varies as a function of particle location within the helicoidal structure of the LC (Figs. 11 and 12). A combination of these effects, e.g., a superposition of periodic dependencies of surface anchoring, elastic, and defect core free energies, gives rise to the potential energy landscape varying as the particle moves

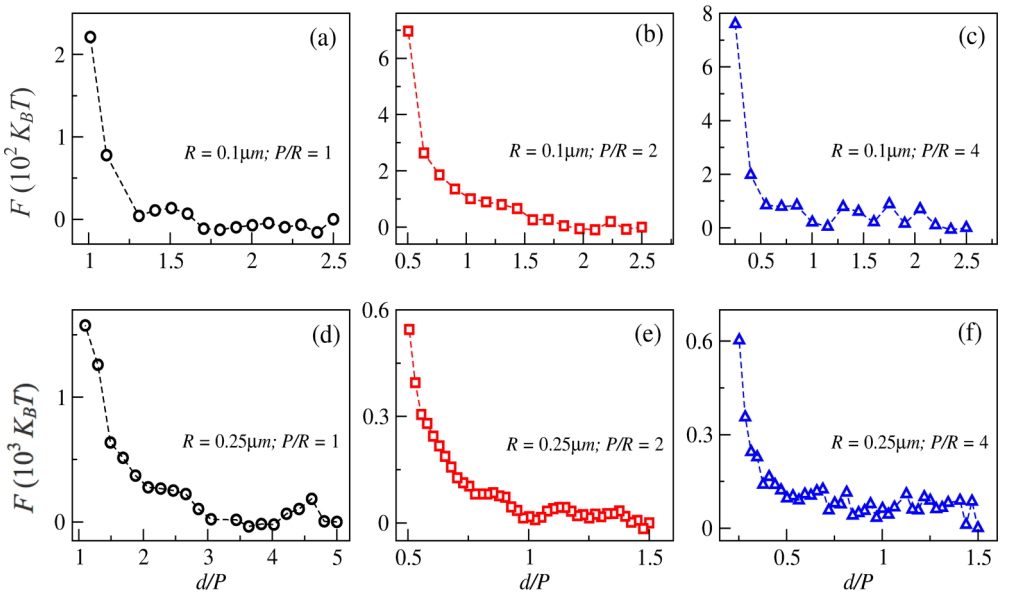

FIG. 10. (Color online) The total free energy as a function of the distance d of a microsphere from a planar cell wall. (a–c) Data for the radius of the particle $R = 0.1\,\mu$m. $L = 2.5P$, $h = 5P$. (d–f) Data for $R = 0.25\,\mu$m. The two sets of data correspond to the cholesteric pitch $P = R, 2R, 4R$, respectively, as marked on the figure parts. (d) $L = 5P$, $h = 10P$; (e, f) $L = 2.5P$, $h = 5P$.

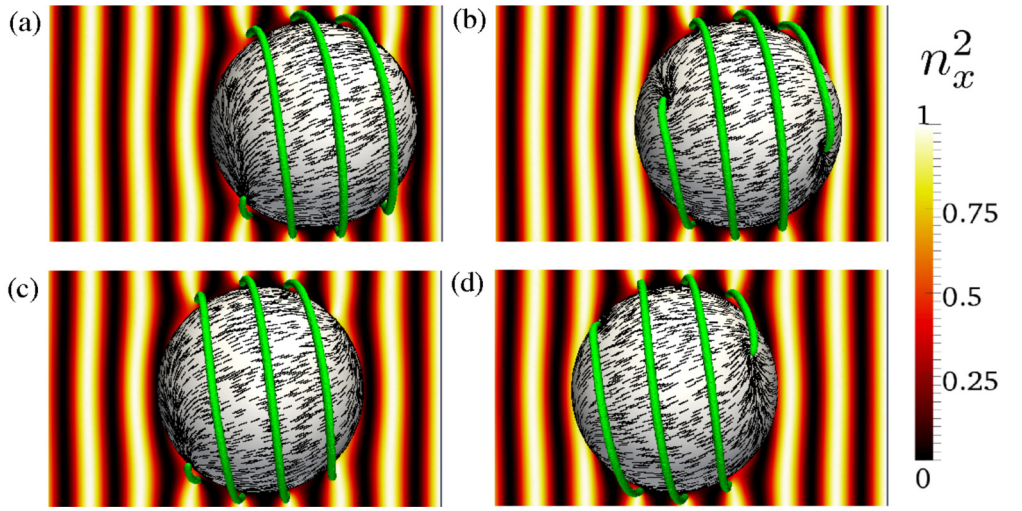

FIG. 11. (Color online) Particle-induced cholesteric structures obtained numerically as a function of the distance d to the wall (at the right). $R = 0.1\,\mu$m, $P = R$, $L = 2.5P$, $h = 5P$. (a) $d = 1.3P$; (b) $d = 1.5P$; (c) $d = 1.8P$; (d) $d = 2.1P$. The color code represents n_x^2, and the isosurfaces of the reduced scalar-order parameter $Q = 0.25$ are shown in green.

along the helical axis, as we observe both experimentally and in numerical modeling. Experimentally, the dependence of free energy due to the colloidal inclusion on its position along the helical axis is further enhanced by anchoring memory effects which cause local transient pinning of the easy axis of the LC director at certain orientations, so that the surface anchoring is nondegenerate. This pinning is promoted by the rough, nonuniform morphology of the particle's surface profile seen in the inset of Fig. 1(b).

Distortions of the cholesteric ground state by an incorporated spherical inclusion can be described in terms of two distortion modes: local perturbations of cholesteric LC order around the particle, and long-range distortions of cholesteric layers far away from the particle. The first type of distortion is accompanied by boojums with an extended core structure, often appearing in the forms of spiraling surface disclinations (Figs. 9, 11, and 12). The perturbations of the cholesteric structure far away from the particle surface can be observed as compressions of cholesteric layers above and below the particle, along with the other boundary-condition-mediated distortions that allow one to match these perturbed parts of the layered structure with the equilibrium one in the rest of the

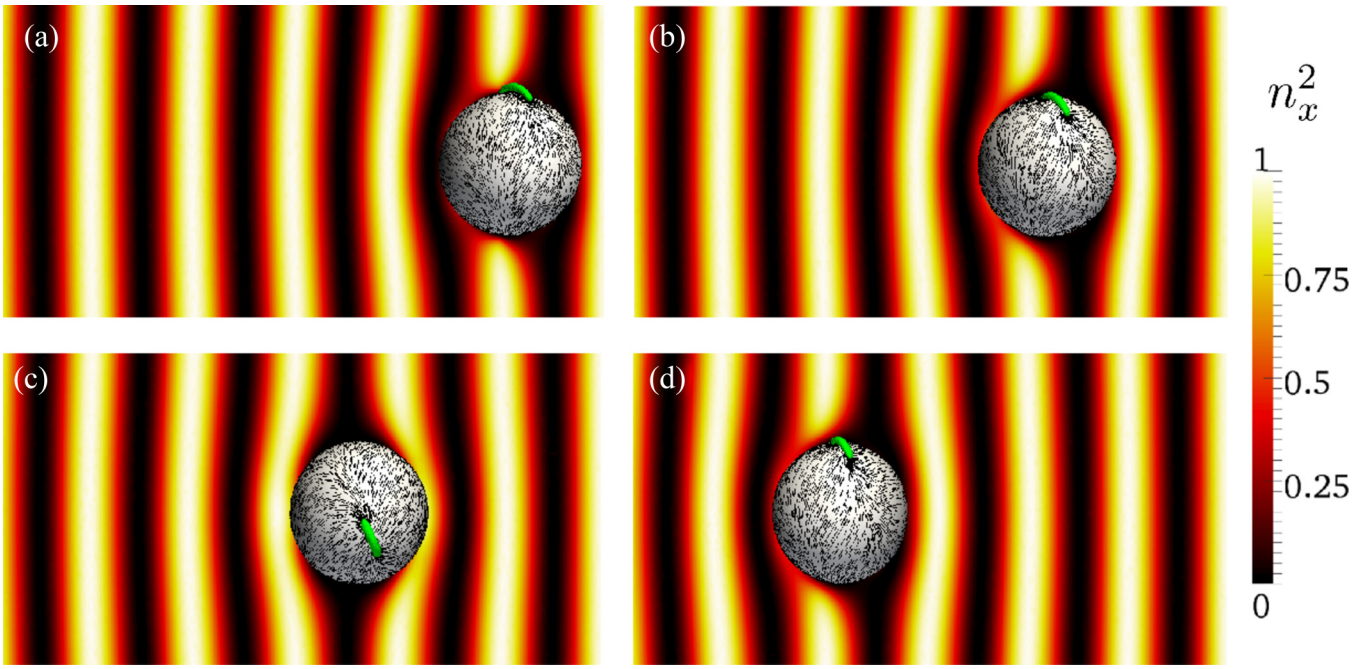

FIG. 12. (Color online) Particle-induced cholesteric structures obtained numerically as a function of the distance d to the wall (at the right). $R = 0.1\,\mu$m, $P = 3R$, $L = 2.5P$, $h = 5P$. (a) $d = 0.48P$; (b) $d = 0.91P$; (c) $d = 1.2P$; (d) $d = 1.92P$. The color code represents n_x^2, and the isosurfaces of the reduced scalar-order parameter $Q = 0.25$ are shown by green color.

sample. The strong elastic distortions and defects immediately around the particle contribute to the periodic potential energy landscape seen by the particle as it moves along the helical axis. On the other hand, long-range distortions of the layered cholesteric structure (mostly compression of layers above and below the sphere, Figs. 11 and 12) further enhance and additionally mediate the observed repulsive interactions with confining surfaces within the LC cell. This combination of elastic forces due to these two types of distortions leads to highly nontrivial motion of particles under the effects of gravity. First, unlike in isotropic fluids, the velocity is not constant and the particle periodically speeds up and slows down while traversing through the cholesteric LC medium due to its interaction with this periodic free-energy landscape, which manifests itself somewhat differently, depending on the shape and the size of the colloidal inclusion relative to the cholesteric pitch (see experimental Figs. 2, 4–8 and theoretical Fig. 9). Second, the particles levitate to some height with respect to the bottom substrate, at which gravity is balanced by elastic repulsive forces due to the perturbation of the cholesteric periodic structure between the particle and the confining wall (Fig. 2). Magnetic and optical holonomic control allowed us to probe these effects in detail, revealing how they depend on shape and size of particles as well as cell and material parameters of the studied system. Furthermore, the strong dependence of the lifetime of metastable states on particle shape and size may potentially be used for particle sorting or for assembling these colloidal particles into long-term stable, three-dimensional arrays within the CLC bulk.

One may ask if the observed metastable states could be possibly a product of stray magnetic fields acting on our SPMB particles, for which most of the reported studies have been performed. However, metastable states were also observed for nonmagnetically functionalized gourd-shaped colloids (as we report elsewhere [41]), melamine resin beads with tangentially degenerate memory-free surface anchoring and rather smooth surfaces, and for GaN nanowires (Fig. 8). These observations effectively rule out stray magnetic fields, although care was taken to null external stray fields in our experiments. Furthermore, our findings are consistent with recent computational studies of spherical colloidal particles in CLCs, which reported metastable states simulated in interparticle interactions in cholesterics as well as in dynamics of nonspherical colloidal particles [32–34].

In future studies, it would be of great interest to explore how the dynamics of colloidal spheres within the bulk CLC samples would be modified if there were no cell confinement, i.e., particles in infinitely large cholesteric samples. In this case, depending on CLC material parameters and the speed and types of particles with tangential anchoring used, one could envision the following possible scenarios: (1) a particle rotating and uniformly translating along the helical axis along with defects and elastic distortions within perturbed or deformed cholesteric layers, with particle and defects effectively behaving as a "larger" colloidal object with an enhanced viscous drag and a larger effective size (this type of behavior is common for nematic colloids [43,44]), or (2) the particle could move while constantly modifying and generating different distortions and defects. The latter type of behavior may be realized in cholesterics because colloidal particles in cholesterics can distort the ground-state cholesteric structures up to distances much larger than the particle size. Experimentally, approaching the confinement-free regime is impossible in rather thick CLC samples with strong surface anchoring on confining surfaces of cells precisely because the distortions of cholesteric periodic structures propagate to distances much larger than the size of colloidal particles, which is due to the medium's lamellarlike behavior. However, working with cells treated for weak surface anchoring [45] may effectively allow one to approach this regime, which will be the subject of future studies.

V. CONCLUSION

We have demonstrated that complex interactions between ground-state helicoidal structures in cholesteric liquid crystals and spherical particles lead to one-dimensional periodic free-energy landscape for a colloidal inclusion's position along a helical axis. This manifests itself in periodic dynamics due to particle motion under the effect of gravity, exhibiting a spectacular departure from Stokes-like behavior known for similar fall experiments in isotropic fluid hosts. We also characterized colloidal levitation in cholesteric cells due to balancing of the gravity by repulsive interactions of the particles with confining cell walls, revealing its dependence on cell and material parameters of colloidal dispersions in CLCs. These experimental observations are consistent with the results of numerical modeling based on the minimization of the Landau–de Gennes free energy, revealing the potential for practical uses in sorting and assembly of colloidal particles of different shapes and sizes and also showing fundamental differences as compared to particle-wall and interparticle interactions in uniformly aligned and twisted nematic liquid crystals [46–50].

ACKNOWLEDGMENTS

We acknowledge discussions with Julian Evans, Bohdan Senyuk, Paul Ackerman, Taewoo Lee, John Price, Chris Twombly, Aric Sanders, and Bennet Schwab. We thank Aric Sanders and acknowledge the use of the NIST imaging facility for obtaining the SEM image of a SPMB particle shown in the inset of Fig. 1(b). This work was supported in part by the NSF Grant No. DMR-0847782 (M.C.M.V. and I.I.S.) and by the U.S. Department of Energy, Office of Basic Energy Sciences, Division of Materials Sciences and Engineering under Award No. ER46921, Contract No. DE-SC0010305 with the University of Colorado (I.I.S.). N.M.S. and M.T. acknowledge partial financial support from the European Union via the 7th Framework International Research Staff Exchange Scheme Marie-Curie Grant No. PIRSES-GA-2010-269181, and from the Portuguese Foundation for Science and Technology (FCT) via Grant No. EXCL/FIS-NAN/0083/2012. N.M.S. also acknowledges partial financial support via FCT Grants No. SFRH/BPD/40327/2007, No. PTDC/FIS/119162/2010, and No. PEstOE/FIS/U10618/2011. Portions of this work related to the fabrication of GaN nanowires contributed by K.A.B. are the contribution of a United States government agency and not subject to copyright.

[1] A. R. Lacey, *Philoponus On Aristotle's Physics* (Duckworth, London, 1993).

[2] E. J. Dijksterhuis, *Simon Stevin: Science in the Netherlands around 1600* (Martinus Nijhoff, The Hague, 1970).

[3] C. G. Adler and B. L. Coulter, Am J. Phys. **46**, 199 (1978).

[4] L. Bod, E. Fischbach, G. Marx, and M. Náray-Ziegler, Acta Phys. Hung. **69**, 335 (1991).

[5] G. L. Smith, C. D. Hoyle, J. H. Gundlach, E. G. Adelberger, B. R. Heckel, and H. E. Swanson, Phys. Rev. D **61**, 022001 (1999).

[6] E. Fischbach and C. L. Talmadge, *The Search for Non-Newtonian Gravity* (Springer, New York, 1999).

[7] D. J. Kapner, T. S. Cook, E. G. Adelberger, J. H. Gundlach, B. R. Heckel, C. D. Hoyle, and H. E. Swanson, Phys. Rev. Lett. **98**, 021101 (2007).

[8] J. C. Long, H. W. Chan, A. B. Churnside, E. A. Gulbis, M. C. M. Varney, and J. C. Price, Nature **421**, 922 (2003).

[9] M. C. M. Varney and J. C. Long, Matters of Gravity **22**, 11 (Fall 2003).

[10] S. Kim and S. J. Karrila, *Microhydrodynamics: Principles and Selected Applications* (Dover Publications, Mineola, NY, 2005).

[11] R. A. Millikan, Phys. Rev. **2**, 109 (1913).

[12] J. C. Loudet, P. Hanusse, and P. Poulin, Science **306**, 1525 (2004).

[13] B. Senyuk, D. Glugla, and I. I. Smalyukh, Phys. Rev. E **88**, 062507 (2013).

[14] D. Engstrom, M. C. Varney, M. Persson, R. P. Trivedi, K. A. Bertness, M. Goksor, and I. I. Smalyukh, Opt. Express **20**, 7741 (2012).

[15] M. C. M. Varney, N. J. Jenness, and I. I. Smalyukh, Phys. Rev. E **89**, 022505 (2014).

[16] D. B. Conkey, R. P. Trivedi, S. R. Pavani, I. I. Smalyukh, and R. Piestun, Opt. Express **19**, 3835 (2011).

[17] H. Dreyfus-Lambez, D. Stoenescu, I. Dozov, and P. Martinot-Lagarde, Mol. Cryst. Liq. Cryst. **352**, 19 (2000).

[18] E. Ouskova, Y. Reznikov, B. Snopok, and A. Tereshchenko, Mol. Cryst. Liq. Cryst. **375**, 97 (2002).

[19] O. O. Ramdane, P. Auroy, S. Forget, E. Raspaud, P. Martinot-Lagarde, and I. Dozov, Phys. Rev. Lett. **84**, 3871 (2000).

[20] D. N. Stoenescu, I. Dozov, and P. Martinot-Lagarde, Mol. Cryst. Liq. Cryst. **351**, 427 (2000).

[21] D. N. Stoenescu, H. T. Nguyen, P. Barois, L. Navailles, M. Nobili, P. H. Martinot-Lagarde, and I. Dozov, Mol. Cryst. Liq. Cryst. **358**, 275 (2001).

[22] Z. G. Forbes, B. B. Yellen, K. A. Barbee, and G. Friedman, IEEE Trans. Magn. **39**, 3372 (2003).

[23] R. M. Erb, N. J. Jenness, R. L. Clark, and B. B. Yellen, Adv. Mater. **21**, 4825 (2009).

[24] Y. Gao, M. A. Hulsen, T. G. Kang, and J. M. J. den Toonder, Phys. Rev. E **86**, 041503 (2012).

[25] Certain commercial materials are identified in this paper only to specify experimental procedures. Such identification implies neither recommendation or endorsement by the National Institute of Standards and Technology, nor that materials identified are necessarily the best available for the purpose.

[26] R. J. S. Derks, A. Dietzel, R. Wimberger-Friedl, and M. W. J. Prins, Microfluid. Nanofluid. **3**, 141 (2007).

[27] S. S. Shevkoplyas, A. C. Siegel, R. M. Westervelt, M. G. Prentiss, and G. M. Whitesides, Lab Chip **7**, 1294 (2007).

[28] Q. Liu, T. Asavei, T. Lee, H. Rubinsztein-Dunlop, S. He, and I. I. Smalyukh, Opt. Express **19**, 25134 (2011).

[29] I. Sinn, T. Albertson, P. Kinnunen, D. N. Breslauer, B. H. McNaughton, M. A. Burns, and R. Kopelman, Anal. Chem. **84**, 5250 (2012).

[30] K. A. Bertness, N. A. Sanford, and A. V. Davydov, IEEE J. Sel. Top. Quantum Electron. **17**, 847 (2011).

[31] V. M. Pergamenshchik and V. A. Uzunova, Phys. Rev. E **79**, 021704 (2009).

[32] V. S. R. Jampani, M. Skarabot, S. Copar, S. Zumer, and I. Musevic, Phys. Rev. Lett. **110**, 177801 (2013).

[33] J. S. Lintuvuori, K. Stratford, M. E. Cates, and D. Marenduzzo, Phys. Rev. Lett. **105**, 178302 (2010).

[34] J. S. Lintuvuori, K. Stratford, M. E. Cates, and D. Marenduzzo, Phys. Rev. Lett. **107**, 267802 (2011).

[35] P. Oswald and P. Pieranski, *Nematic and Cholesteric Liquid Crystals: Concepts and Physical Properties Illustrated by Experiments* (Taylor & Francis/CRC Press, Boca Raton, FL, 2005).

[36] P. G. de Gennes and J. Prost, *The Physics of Liquid Crystals*, 2nd ed. (Clarendon, Oxford, 1993).

[37] J. B. Fournier and P. Galatola, Europhys. Lett. **72**, 403 (2005).

[38] M. Tasinkevych, N. M. Silvestre, and M. M. Telo da Gama, New J. Phys. **14**, 073030 (2012).

[39] H. Grebel, R. M. Hornreich, and S. Shtrikman, Phys. Rev. A **28**, 1114 (1983).

[40] R. P. Trivedi, I. I. Klevets, B. Senyuk, T. Lee, and I. I. Smalyukh, Proc. Natl. Acad. Sci. USA **109**, 4744 (2012)

[41] B. Senyuk, M. Varney, J. Lopez, S. Wang, N. Wu, and I. I. Smalyukh, Soft Matter **10**, 6014 (2014).

[42] N. Hijnen, T. A. Wood, D. Wilson, and P. S. Clegg, Langmuir **26**, 13502 (2010).

[43] H. Stark, Eur. Phys. J. B **10**, 311 (1999); Phys. Rep. **351**, 387 (2001).

[44] H. Stark and D. Ventzki, Phys. Rev. E **64**, 031711 (2001).

[45] I. I. Smalyukh and O. D. Lavrentovich, Phys. Rev. Lett. **90**, 085503 (2003).

[46] C. Lapointe, A. Hultgren, D. M. Silevitch, E. J. Felton, D. H. Reich, and R. L. Leheny, Science **303**, 652 (2004).

[47] C. Lapointe, N. Cappallo, D. H. Reich, and R. L. Leheny, J. Appl. Phys. **97**, 10Q304 (2005).

[48] J. B. Rovner, D. H. Reich, and R. L. Leheny, Langmuir **29**, 2104 (2013).

[49] O. P. Pishnyak, S. Tang, J. R. Kelly, S. V. Shiyanovskii, and O. D. Lavrentovich, Phys. Rev. Lett. **99**, 127802 (2007).

[50] J. Kotar, M. Vilfan, N. Osterman, D. Babič, M. Čopič, and I. Poberaj, Phys. Rev. Lett. **96**, 207801 (2006).